JOURNAL OF THE AMERICAN CHEMICAL SOCIETY

Subscriber access provided by Stockholm University Library

Article

Cooperative Stabilization of the [Pyridinium-CO-Co] Adduct on a Metal–Organic Layer Enhances Electrocatalytic CO Reduction

Ying Guo, Wenjie Shi, Huijuan Yang, Quanfeng He, Zhongming Zeng,
Jin-yu Ye, Xinru He, Ruiyun Huang, Cheng Wang, and Wenbin Lin

J. Am. Chem. Soc., **Just Accepted Manuscript** • DOI: 10.1021/jacs.9b09227 • Publication Date (Web): 11 Oct 2019

Downloaded from pubs.acs.org on October 12, 2019

Just Accepted

“Just Accepted” manuscripts have been peer-reviewed and accepted for publication. They are posted online prior to technical editing, formatting for publication and author proofing. The American Chemical Society provides “Just Accepted” as a service to the research community to expedite the dissemination of scientific material as soon as possible after acceptance. “Just Accepted” manuscripts appear in full in PDF format accompanied by an HTML abstract. “Just Accepted” manuscripts have been fully peer reviewed, but should not be considered the official version of record. They are citable by the Digital Object Identifier (DOI®). “Just Accepted” is an optional service offered to authors. Therefore, the “Just Accepted” Web site may not include all articles that will be published in the journal. After a manuscript is technically edited and formatted, it will be removed from the “Just Accepted” Web site and published as an ASAP article. Note that technical editing may introduce minor changes to the manuscript text and/or graphics which could affect content, and all legal disclaimers and ethical guidelines that apply to the journal pertain. ACS cannot be held responsible for errors or consequences arising from the use of information contained in these “Just Accepted” manuscripts.

is published by the American Chemical Society. 1155 Sixteenth Street N.W., Washington, DC 20036

Published by American Chemical Society. Copyright © American Chemical Society. However, no copyright claim is made to original U.S. Government works, or works produced by employees of any Commonwealth realm Crown government in the course of their duties.

Cooperative Stabilization of the [Pyridinium-CO_2-Co] Adduct on a Metal–Organic Layer Enhances Electrocatalytic CO_2 Reduction

Ying Guo,[†,#] Wenjie Shi,[†,#] Huijuan Yang,[†] Quanfeng He,[†] Zhongming Zeng,[†] Jin-yu Ye,[†] Xinru He,[†]
Ruiyun Huang,[†] Cheng Wang*,[†] and Wenbin Lin[†,‡]

[†]State Key Laboratory of Physical Chemistry of Solid Surfaces, iCHEM, College of Chemistry and Chemical Engineering, Xiamen University, Xiamen 361005, P.R. China

[‡]Department of Chemistry, The University of Chicago, 929 East 57th Street, Chicago, Illinois 60637, United States

Supporting Information Placeholder

ABSTRACT: Pyridinium has been shown as a co-catalyst for electrochemical reduction of CO_2 on metal and semiconductor electrodes but its exact role has been difficult to elucidate. In this work, we create cooperative cobalt-protoporphyrin (CoPP) and pyridine/pyridinium (py/pyH$^+$) catalytic sites on metal-organic layers (MOLs) for electrocatalytic CO_2 reduction reaction (CO_2RR). Constructed from $[Hf_6(\mu_3\text{-}O)_4(\mu_3\text{-}OH)_4(HCO_2)_6]$ secondary building units (SBUs) and terpyridine-based tricarboxylate ligands, the MOL was post-synthetically functionalized with CoPP via carboxylate exchange with formate capping groups. The CoPP group and the pyridinium (pyH$^+$) moiety on the MOL coactivate CO_2 by forming the [pyH$^+$-^-O_2C-CoPP] adduct, which enhances CO_2RR and suppresses hydrogen evolution to afford a high CO/H_2 selectivity of 11.8. Cooperative stabilization of the [pyH$^+$-^-O_2C-CoPP] intermediate led to a catalytic current density of 1314 mA/mgCo for CO production at -0.86 V_{RHE}, which corresponds to a turnover frequency of 0.4 s^{-1}.

INTRODUCTION

Converting CO_2 into useful chemicals using electricity from solar and other renewable energy sources is one of the most active areas of current research.[1-6] To achieve high Faradaic efficiency (FE) in a CO_2 reduction reaction (CO_2RR), the competing hydrogen evolution reaction (HER) must be suppressed at the requisite negative potential for CO_2RR.[7-8] The pyridine/pyridinium (py/pyH$^+$) species has been reported as a co-catalyst for electrochemical CO_2RR on various metal and semiconductor electrodes.[9-13] Similarly, nitrogen doped carbons (N-Cs) with pyridinic nitrogen are effective for CO_2RR with high FEs.[14-15] The exact role of py/pyH$^+$ is still under investigation.[16-20]

For example, theoretical calculations revealed a 1,2-dihydropyridine (pyH_2) as a possible intermediate mimicking the NADPH in the natural photosynthesis to transfer a hydride to CO_2 for its reduction, but experimental attempts to directly detect this intermediate or related D/H exchange species in isotope experiment have failed.[17] On the other hand, the electro-generation of pyridinyl radical (pyH$^•$) was also proposed as the electron shuttle for CO_2 reduction; such π-radicals were observed by electron paramagnetic spectroscopy (EPR) and UV-Vis spectroscopy for 4,4'-bipyridinium in aqueous solution using a Pt working electrode, but the calculated redox potential of pyH$^•$ appears to be too negative for its participation in the reaction.[19] In an alternative explanation, the pyridinium can assist the formation of hydride on the electrode surface to steer selectivity towards CO_2RR by modulating the microenvironment around the catalytic centers on the electrode.[19]

If the promoting effect of py/pyH$^+$ can be generalized to molecular CO_2RR catalysts, we conjectured that molecular materials with well-defined catalytic sites would be ideally suited for pinpointing the role of py/pyH$^+$ in CO_2RR. Herein we report the study of py/pyH$^+$ in enhancing CO_2RR by a cobalt-porphyrin electrocatalyst in a metal-organic layer (MOL).

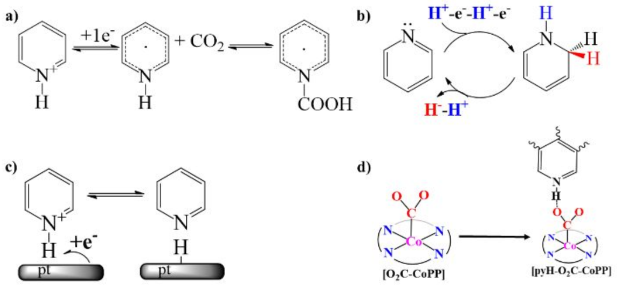

Figure 1. Different views on the function of the py/pyH$^+$ species in CO_2RR: a) Pyridinium reduction by one electron, forming the pyridinyl radical, followed by its reaction with CO_2 to form a radical carbamate;[19] b) Formation of 1,2-Dihydropyridine (PyH_2) from PyH^0 via successive 1H$^+$/1e$^-$ transfers;[17] c) Inner-Sphere reduction of a pyrH$^+$-bound proton on a Pt Electrode to form a surface hydride;[19] d) Cooperative activation of CO_2 by CoPP and pyH$^+$ in this work.

As a monolayer version of two-dimensional metal-organic frameworks (MOFs), MOLs have recently been developed as a novel class of functional molecular materials.[21-23] MOLs are ideally suited for electrocatalysis as their ultrathin nature overcomes the conductivity constraint in MOFs.[24] The distances for electron migration and counterion movement are quite short through a monolayer, enabling the use of MOLs as effective electrocatalysts.[25] MOLs also allow for controlling microenvironment around catalytic centers through surface modification of the secondary building units (SBUs).[26]

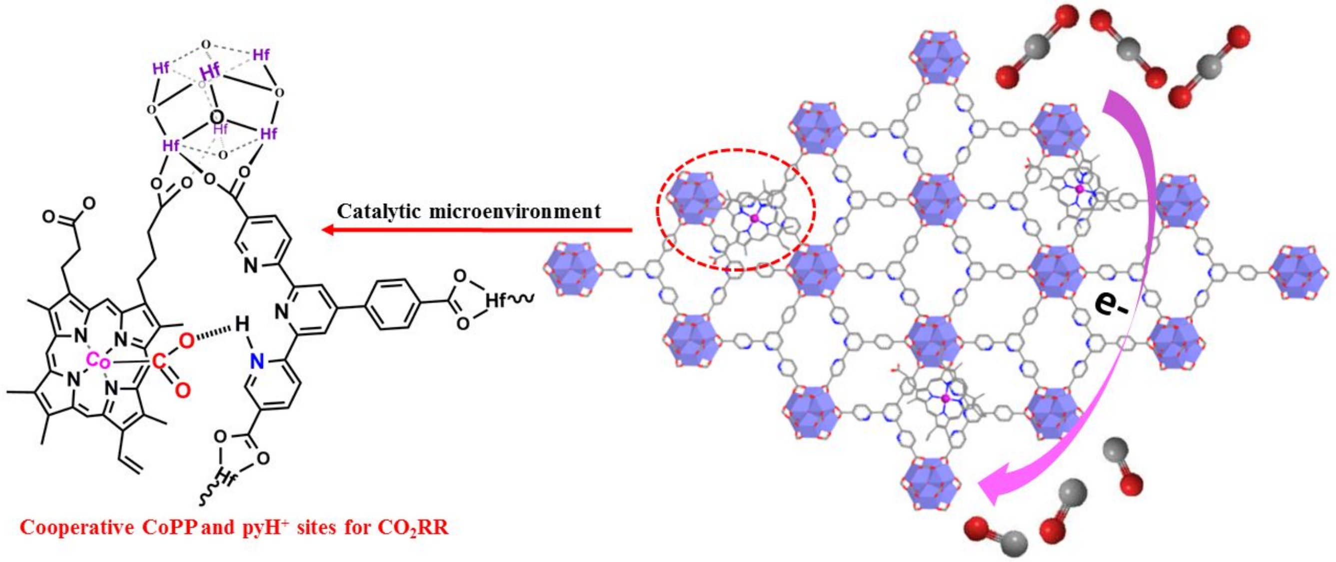

Figure 2. Schematic showing the structure of TPY-MOL-CoPP and cooperative activation of CO_2 by CoPP and pyH^+.

In this work, we used MOLs as a 2D scaffold to tune the microenvironment of the Co-protoporphyrin (CoPP) electrocatalyst for CO_2RR in aqueous media. CoPP was post-synthetically installed on the $[Hf_6(\mu_3\text{-}O)_4(\mu_3\text{-}OH)_4(HCO_2)_6]$ SBUs of BTB-MOL and TPY-MOL built from triangular benzenetribenzoate (BTB) and 4'-(4-benzoate)-(2,2',2''-terpyridine)-5,5''-dicarboxylate (TPY) linkers, respectively,[26] via carboxylate exchange with formate capping groups on the MOLs (Figure 1). Changing the microenvironment around CoPP from phenyl rings in BTB to py moieties in TPY significantly enhanced electrocatalytic CO_2RR, increasing CO/H_2 current density ratios from 2.7 in BTB-MOL-CoPP to 11.8 in TPY-MOL-CoPP at an electrolysis potential of -0.86 V *vs.* reversible hydrogen electrode (V_{RHE}).

RESULTS AND DISCUSSION

Catalyst Synthesis and Characterization

BTB-MOL and TPY-MOL with the compositions of $[Hf_6(\mu_3\text{-}O)_4(\mu_3\text{-}OH)_4(HCO_2)_6(L)_2]$ (L=BTB and TPY, respectively) were synthesized following our previous report.[23] The MOLs were then functionalized with CoPP in DMF at 60℃. The methylene bridge between the carboxylate linker and the porphyrin moiety in CoPP gives flexibility to the structure to better accommodate CO_2 as a substrate. Such flexible linkages are widely utilized in many enzymes to allow for "induced fit" between the catalytic center and the substrate.[27-28] We hypothesized that these structural features would lead to cooperativity between TPY and CoPP in electrocatalytic CO_2RR.

The MOLs appeared as wrinkled ultrathin films by transmission electron microscopy (TEM) (Figure 2a, Figure S1 & S2). Their powder X-ray diffraction (PXRD) patterns were consistent with a structure of 3,6-connected 2D net of alternatively linked tricarboxylate ligands and Hf_6 SBUs of the *kgd* topology (Figure 2b, Figure S3). Atomic force microscopy (AFM) showed a thickness of 1.2±0.2 nm for the as-synthesized TPY-MOL (Figure S1), which corresponds to the van der Waals diameter of Hf_6 SBUs and suggests the monolayer structure of the MOL.

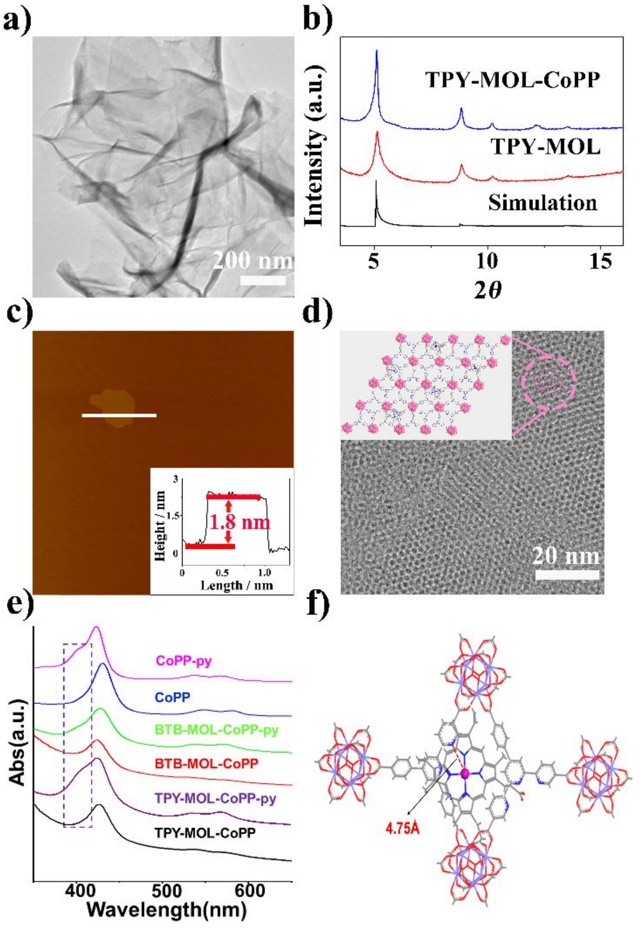

Figure 3. a) TEM images of TPY-MOL-CoPP. b) PXRD patterns of TPY-MOL and TPY-MOL-CoPP. c) AFM and d) HRTEM images of TPY-MOL-CoPP. e) UV-Vis spectroscopy of CoPP, CoPP coordinated with pyridine, BTB-MOL-CoPP, BTB-MOL-CoPP with additional pyridine and TPY-MOL-CoPP, and TPY-MOL-CoPP with additional pyridine. f) Optimization of a structural model of TPY-MOL-CoPP, showing the closest distance between the Co and a N on the terpyridine.

The amounts of adsorbed CoPP were quantified to be 8.4 wt% for BTB-MOL-CoPP and 5.5 wt% for TPY-MOL-CoPP by UV-Vis spectroscopy (Figure S4), which correspond to CoPP/Hf_6 SBU ratios of 0.32 and 0.17, respectively (Table S1). TEM images and PXRD patterns of the modified samples were very similar to that of the as-synthesized MOLs, confirming structure stability during the modification (Figures 2a & 2b, Figures S1-3). PXRD patterns of TPY-MOL-CoPP recovered from suspensions in N_2-saturated 0.1 M buffer solution of NaH_2PO_4/Na_2HPO_4 and CO_2-saturated 0.1 M $NaHCO_3$ solution confirmed structure stability in the electrolytic solution (Figure S5). AFM measurements of TPY-MOL-CoPP gave a thickness of 1.8±0.2 nm (Figure 2c), which is slightly thicker than that of the unmodified one (1.2±0.2 nm) due to the steric bulk of CoPP.

It is important to consider if the pyridine moiety on the TPY can directly coordinate to the Co center on the CoPP in the TPY-MOL-CoPP. The structural modelling of the CoPP catalytic center by Materials Studio software showed that the steric bulk of the terpyridine and the MOL SBUs prevent such a coordination (Figure 3f). Molecular mechanics optimization (using universal force field for MOF) of a structural model beginning with a forced coordination between the Co and a N on the terpyridine led to the cleavage of the coordination bond due to the steric repulsion between the CoPP and the TPY moieties. The resulting structure has a shortest Co-N distance of 4.75Å that is beyond the range of a coordination bond (Figures S6 & S7). Furthermore, a careful study of the UV-Vis spectra of a series of MOL-CoPP composites also ruled out such a coordination (Figure 3e). The UV-Vis spectrum of the pyridine-treated CoPP molecule (CoPP-py) or BTB-MOL-CoPP sample (BTB-MOL-CoPP-py) showed an additional shoulder at around 400 nm to the blue side of the Soret absorption band of the CoPP in BTB-MOL-CoPP, which is characteristic of the CoPP-py moiety. However, this spectrum feature is absent in the UV-Vis of the TPY-MOL-CoPP. On the other hand, treating the TPY-MOL-CoPP with additional free pyridine generates similar features of CoPP-py in the UV-Vis spectrum. All of these observations support a lack of pyridine coordination to Co in the TPY-MOL-CoPP sample.

Catalytic Activity

The CO_2RR activities of the MOL catalysts were measured in CO_2-saturated aqueous solution of 0.1M $NaHCO_3$ in an air-tight H-type cell with Nafion membranes separating working and counter electrodes. The MOLs were stable in the buffer solution as revealed by the retention of their PXRD patterns (Figure S5). The MOL-CoPP samples were loaded onto carbon cloth by drop-drying. Electrolysis was performed in the potential range of -0.56 to -0.86 V_{RHE}. CO and H_2 were detected by online gas chromatography (GC). No liquid products were detected by ^1H NMR spectra taken at the completion of each electrolysis. The catalytic current densities for CO (j_{CO}) and H_2 (j_{H2}) were calculated according to the amounts of H_2 and CO generated with respect to the quantities of charge passed in electrolysis. The Faradaic efficiencies (FEs) were calculated as the ratios between the partial current densities and the total current densities (j_{total}).

At -0.86 V_{RHE}, BTB-MOL-CoPP showed a j_{CO} of 923 mA/mg (Figure S8) on a per cobalt basis with j_{CO}/j_{H2} ratio of 2.7 while TPY-MOL-CoPP exhibited a j_{CO} of 1314 mA/mg with a much higher j_{CO}/j_{H2} ratio of 11.8 (Figure 4a). TPY-MOL-CoPP gave a CO-FE of 92.2% (Figure 4a) and a turnover frequency of 0.40 s^{-1}. Such an activity is much higher than those of many other porphyrin-based electrocatalysts for CO_2 conversion to CO (Figure 4b).[2,29-31] At lower potentials, TPY-MOL-CoPP also showed higher CO-FE than BTB-MOL-CoPP (Figure 4c). Control experiments using TPY-MOL and BTB-MOL without CoPP functionalization showed only HER (Figure S9), demonstrating that CoPP is the catalytic center.

The promoting effect of the TPY ligand for CO_2RR was verified in a poisoning experiment by coordinating the TPY site with Zn^{2+} or Ca^{2+}, which significantly reduced the CO-FE from 92.2% to 6% and 8%, respectively (Figure 4a). Consistent with our analysis, the promoting effect of TPY is not due to pyridine coordination to the Co center in CoPP because the addition of pyridine to the solution led to a significantly reduced CO-FE to 29% (Figure 4a). The promoting effect of the TPY was observed at all potentials (Figure 4c, Figures S8 & S10).

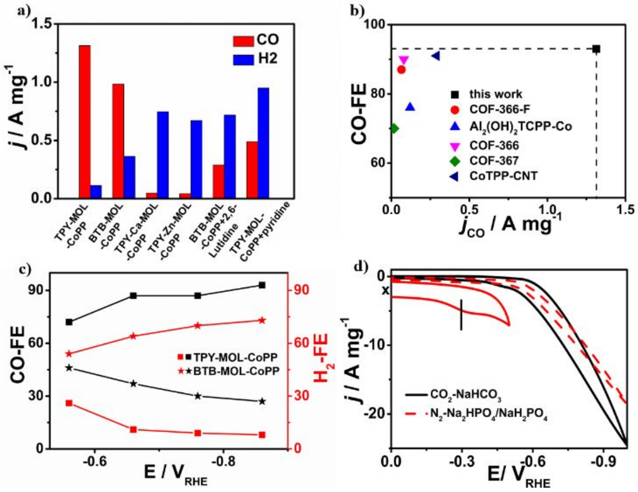

Figure 4. a) Current densities per mg of cobalt for different MOL-CoPP catalysts at an applied potential of −0.86 V_{RHE} in CO_2-saturated 0.1M $NaHCO_3$ aqueous solution; b) Comparison of CO_2RR catalytic performances of different Co-porphyrin based catalysts. X axis represents current density on a per mg cobalt basis while Y axis represents CO-FE. c) Faradaic efficiency for CO and H_2 *vs.* the electrolysis potential for different catalysts in CO_2-saturated 0.1 M $NaHCO_3$ d), Cathodic wave (CV) of TPY-MOL-CoPP in CO_2-saturated 0.1M $NaHCO_3$ (black solid lines) and in N_2-saturated 0.1 M NaH_2PO_4/Na_2HPO_4 (reddashed lines), Enlarged Cathodic wave (CV) of TPY-MOL-CoPP in N_2-saturated 0.1 M NaH_2PO_4/Na_2HPO_4 at scan rate of 200 mv/s (red solid lines).

To understand the origin of the CO_2RR *vs.* HER selectivity, we compared electrocatalysis in CO_2-saturated aqueous solution of 0.1 M $NaHCO_3$ at pH=6.8 and in N_2-saturated NaH_2PO_4/Na_2HPO_4 buffer solutions at pH=6.8. Both TPY-MOL-CoPP and BTB-MOL-CoPP showed higher current densities in CO_2-saturated solutions (j_{inCO2}) than those in N_2-saturated solutions (j_{inN2}). The j_{inCO2} values contain current densities for both HER and CO_2RR while the j_{inN2} values are entirely from HER (Figure S11, Table S2). However, the (j_{inCO2} - j_{inN2})/j_{inCO2} ratios are much lower than the FEs for CO_2RR at various potentials for both MOL catalysts. This result suggests that HER is suppressed in the presence of CO_2RR. Consistent with this, the current densities for HER (j_{H2}) in CO_2-saturated solution is much lower than those in N_2-saturated solution (Tables S2 & S3). This suppression of HER is likely due to CO_2RR and HER competing for the same catalytic sites. We note that it may also result from the higher local pH in the CO_2RR with $CO_2/HCO_3^-/CO_3^{2-}$ buffer than that in the N_2

atmosphere with NaH_2PO_4/Na_2HPO_4 buffer. The j_{H2} value for TPY-MOL-CoPP is similar to the background current density of the carbon cloth without loading any catalyst. The HER of TPY-MOL-CoPP under CO_2 atmosphere thus mainly comes from the carbon cloth, indicating that the intrinsic CO/H_2 selectivity of the CoPP site in TPY-MOL-CoPP should be even higher than the measured value of 11.8.

A reductive peak at ~-0.28 V_{RHE} can also be found on the CV scan of the TPY-MOL-CoPP under the N_2 atmosphere with NaH_2PO_4/Na_2HPO_4 buffer when the scan rate was 200 mV/s (Figure 4d, Figure S12). This peak is assigned to the reduction of $[CoPP]^0$ to $[CoPP]^-$. The CO_2RR and the HER both happen at more negative onset potentials than -0.28 V_{RHE}, which should correspond to the potentials for the injection of the second electrons.

Local pH and Mass Transport in Electrolysis

To reveal the function of the pyridine promoter, we first examined the possibility for the pyridine group to affect local pH or the mass transport of CO_2.

As a result of a fast consumption of proton or generation of hydroxide in the electrocatalytic CO_2RR and HER processes, the solution around the electrode surface can exhibit significantly higher local pH than the bulk solution (Figure 5a). Both CO_2RR and HER processes consume one proton or generate one hydroxide while obtaining one electron. We can thus build up a general relationship between the local pH and the catalytic current density with a given concentration of the buffering species.

The CO_2/HCO_3^- pair is not an efficient buffer pair due to its slow kinetics in proton transfer. The rate of CO_2 dissociation to generate HCO_3^- and proton is around 0.0371 s^{-1},[32] which can give local protons at a maximum rate of 3.7×10^{-9} mol cm^{-2} s^{-1} considering a liquid layer of 30 μm in thickness around the electrode and a saturated CO_2 concentration of ~34 mM (thus 1×10^{-7} mol cm^{-2} of CO_2 near the electrode) as a "local" reservoir. This possible maximum rate is still much lower than the rate of proton consumption in the electrocatalytic CO_2RR with a current density over 1 mA/cm^2 (~1×10^{-8} mol cm^{-2} s^{-1} proton consumption). As a result, we can ignore the conversion of CO_2 to HCO_3^- at the "local" environment around the electrode as a proton generation source in the electrocatalysis in a rough estimation. Similarly, the rate of water dissociation to produce H^+ and OH^- is not fast enough (2.4×10^{-5} M s^{-1}) to provide proton (7.2×10^{-11} mol cm^{-2} s^{-1} proton generation rate in 30 μm liquid layer) for the proton consumption in the electrolysis.

At steady state, the consumed proton at the electrode should be provided by the diffusion and the equilibrium of hydronium (H_3O^+), hydroxide (OH^-), bicarbonate/carbonate (HCO_3^-/CO_3^{2-}). Because of the low bulk concentration of H_3O^+ ($10^{-6.8}$ M) and OH^- ($10^{-7.2}$ M) in the bulk solution at pH 6.8 as compared to the concentration of HCO_3^- (0.1 M), the contribution from H_3O^+ and OH^- diffusion can be ignored. The conversion between HCO_3^- and CO_3^{2-} is fast enough with a rate constant of 59.44 s^{-1} [32] that corresponds to a maximum local proton generation rate of 1.8×10^{-5} mol cm^{-2} s^{-1} considering a liquid layer of 30 μm in thickness. We can thus simplify the analysis by considering the HCO_3^- as the only proton carrier in the reaction.

Combining the mass conservation of proton at the steady-state condition with the Fick's diffusion law, we can obtain

$$\frac{j_{total}}{F} = -D_{HCO_3^-}\frac{\partial[HCO_3^-]}{\partial x}\bigg|_{x=0} = D_{HCO_3^-}\frac{[HCO_3^-]_{bulk}-[HCO_3^-]_{local}}{l} \quad (1)$$

Where the D is the diffusivity of bicarbonate, l is the effective thickness of the diffusing layer.

Because we ignored the hydration of CO_2 in the proton balance, the sum of the flux of bicarbonate and carbonate is a constant at the steady state due to mass conservation.

$$D_{HCO_3^-}\frac{\partial[HCO_3^-]}{\partial x} + D_{CO_3^{2-}}\frac{\partial[CO_3^{2-}]}{\partial x} = 0 \quad (2)$$

Combining these mass conservation equations with the equilibrium equation between the carbonate and bicarbonate

$$\frac{[HCO_3^-]_{local}}{[CO_3^{2-}]_{local}} = \frac{[H^+]_{local}}{K_{a2}} \quad (3)$$

We can obtain (see SI for more details)

$$pH_{local} = pH_{bulk} + \log\left(1 + \frac{j_{total}}{j_d}\right) \quad (4)$$

Where $j_d = F \times D_{CO_3^{2-}}[CO_3^{2-}]_{bulk}/l$ (5)

The local pH of CO_2RR with stirring in the solution has been measured by Xu et al using electrochemical diffuse reflectance Infrared Fourier transform spectroscopy (DRIFTS)[33] which estimates the local pH from the concentration ratio between the carbonate and bicarbonate. Fitting the equation with data from the reference[33] gives an effective diffusing layer thickness of l=31 μm (Figure 5b). Such a diffusing layer thickness is reasonable for a system with mechanical stirring in the solution.[34]

The rate of CO_2 mass transport can be estimated by a $^{13}CO_2$ exchange experiment. $^{13}CO_2$ gas was filled in the headspace of the vial with 0.1 M $NaH^{12}CO_3$ electrolyte under vigorous stirring either in the presence or in the absence of TPY-MOL-CoPP in the solution. An on-line mass spectrometry (MS) measured the $^{13}CO_2$ / $^{12}CO_2$ ratio in the headspace as a function of time (Figure S13), the kinetic curve of which reflects the rate of CO_2 transfer between the gas and the liquid phase to give a specific mass transport coefficient of (0.0015±0.0002) s^{-1} that corresponds to a CO_2 feeding rate of ~1.5×10^{-6} mol s^{-1} giving the total solution volume of 30 mL, far exceeding the CO_2 consumption rate at the electrode (~1×10^{-8} mol s^{-1} for a current density of 1 mA/cm^2 and an electrode area of 1 cm^2). This proves that the CO_2 transport from the gas phase to the liquid phase does not present a limitation on the electrolysis, and we can thus assume a saturated CO_2 concentration of 34 mM in the bulk solution. Combining this concentration with the CO_2 diffusivity of 1.9×10^{-9} m^2/s and a required CO_2 transport flux of 1×10^{-8} mol cm^{-2} s^{-1} (1mA/cm^2) to the electrode, the CO_2 concentration at the electrode should still be 32.4 mM assuming a diffusing layer of 30 μm in thickness. As a result, the CO_2 transport is not likely to be a limitation to the CO_2RR in the current experimental setup.

To validate the above assumptions in deriving the equation for local pH and to corroborate with the CO_2 diffusion analysis, we also performed numerical simulations by COMSOL Multiphysics v4.3b software[32,35] using the diffusivities of different species and the reaction rates among them (without adopting the above assumption of ignoring CO_2 dissociation process). The dominant role of HCO_3^- as the H-carrier was confirmed in the simulation and the local pH values obtained from the simulation are very similar to those predicted from Equation 4 (Figure 5b-d).

A typical local pH of ~8.0 was obtained for the CO_2RR at a current density of ~1 mA/cm^2 and a $NaHCO_3$ concentration of 0.1 M in the CO_2 saturated solution. This local pH is well above the pKa of pyridinium/pyridine of 4-6. The buffering effect of the pyridinium/pyridine at the local pH is thus negligible since all the free pyridine should be in the deprotonated form. As these pyridine/pyridinium moieties are fixed on the electrode surface without continuous transportation of pyridinium from the bulk solution, they cannot serve as a bulk pyridine/pyridinium buffer and have no effect on the local pH at the steady state.

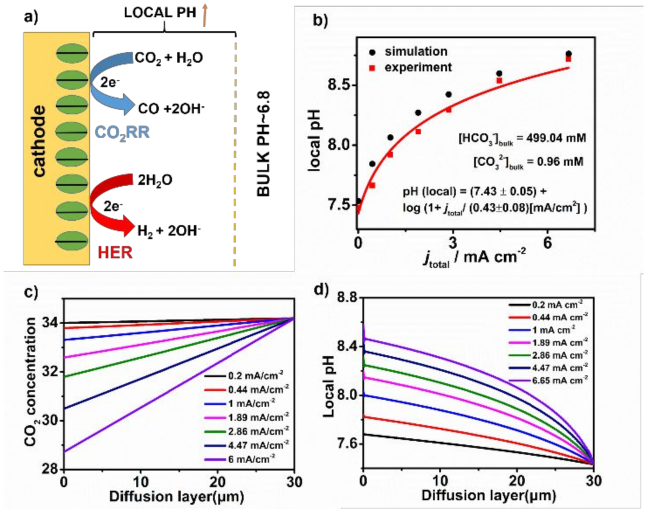

Figure 5. a) The build-up of local pH near the electrode due to CO_2RR and HER. b) The fitted equation of the local pH in CO_2RR using COMSOL and experimental local pH from the reference[33] together with the fitting from Equation 4, with 0.5 M of HCO_3^- in the electrolytes. c) CO_2 concentration distribution at different steady state conditions from COMSOL simulation. d) Local pH distribution at steady state conditions from COMSOL simulation.

Kinetic Studies and the Apparent Rate Law

We have changed the partial pressure of CO_2 and the concentration of HCO_3^- in the solution to study the dependence of the CO and H_2 current densities on these parameters. Different amounts of NaCl or Na_2HPO_4 were also added to the solution in addition to the $NaHCO_3$ to keep the Na^+ concentration the same in all of the tests (Tables S4 & S5). We must note that the change of the CO_2 partial pressure and the HCO_3^- concentration also changes the bulk pH of the system and the local pH around the catalytic electrode. The addition of Na_2HPO_4 leads to an additional buffering pair $H_2PO_4^-/HPO_4^{2-}$ with a pKa of 7.21 to affect both bulk and local pH. The pH of the bulk solution ranges from 6.42 to 7.42 in these experiments, while the local pH around the electrode ranges from 6.42 to 9.32 according to Equation 4.

The CO current density increases with both increasing CO_2 partial pressure and increasing HCO_3^- concentration (Figure 6a-b). We can obtain an apparent rate law of CO_2RR (Figure 6c-d) for the TPY-MOL-CoPP catalyst as

$$j_{CO} = 11900\ \mathrm{mA\ mg^{-1}M^{-1}} \times \left([HCO_3^-] + 0.041M\right) \times \frac{[CO_2]}{[CO_2] + 0.011M} \quad (6)$$

The apparent rate law of CO_2RR for the BTB-MOL-CoPP catalyst is

$$j_{CO} = 7000\ \mathrm{mA\ mg^{-1}M^{-1}} \times \left([HCO_3^-] + 0.059M\right) \times \frac{[CO_2]}{[CO_2] + [H^+]_{local}/10^{-4.9}}$$

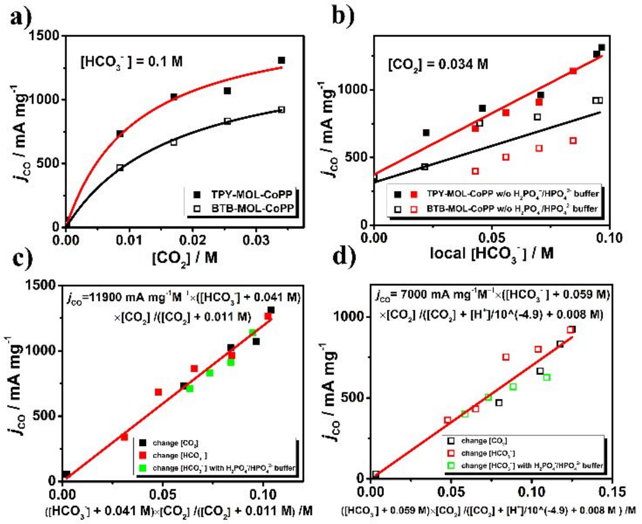

Figure 6. a) Dependence of CO current density on the CO_2 concentration (changing p_{CO2}) in the bulk solution at a constant potential of -0.86V_{RHE} for TPY-MOL-CoPP and BTB-MOL-CoPP ; b) Dependence of CO current density on HCO_3^- concentration at a constant potential of -0.86V_{RHE} for TPY-MOL-CoPP and BTB-MOL-CoPP (black square: with different $H_2PO_4^-/HPO_4^{2-}$ buffer concentrations for TPY-MOL-CoPP; red square: tuning HCO_3^- concentration without adding $H_2PO_4^-/HPO_4^{2-}$ buffer for TPY-MOL-CoPP; black hollow square: with different $H_2PO_4^-/HPO_4^{2-}$ buffer concentrations for BTB-MOL-CoPP; red hollow square: tuning HCO_3^- concentration without adding $H_2PO_4^-/HPO_4^{2-}$ buffer for BTB-MOL-CoPP.c)-d) The rate laws of CO_2RR for the TPY-MOL-CoPP and BTB-MOL-CoPP catalysts, with experimental data from tuning the CO_2 concentration by changing p_{CO2} (black), tuning the HCO_3^- concentration (red) and adding different concentrations of the $H_2PO_4^-/HPO_4^{2-}$ buffer (green).

These two similar rate laws of TPY-MOL-CoPP and BTB-MOL-CoPP indicate that the pyridine moiety in TPY-MOL-CoPP may not change the catalytic path of the CoPP catalyst but significantly tunes the reaction rate or the equilibrium among related species in the elementary steps. The dependence of the reaction rate on the local concentration of bicarbonate suggests that there is a HCO_3^--assisted path acting as the major turnover path when the HCO_3^- concentration is above 0.1 M. The Langmuir type dependence on the CO_2 concentration suggests an equilibrium of an active CO_2-adsorbed species with other CO_2-related species in the system. This species is likely to be the one before the rate-determining step (RDS), in other words, the resting state of the catalyst-CO_2 assembly.

in situ Electrochemical Diffuse Reflectance Infrared Fourier Transform Spectroscopy

We then performed *in situ* electrochemical DRIFTS in an attempt to capture the resting state species before the RDS and to gain further insight into the role of py/pyH^+ in CO_2RR (Figure 7a). When the potential was scanned to the negative direction, the differential spectra of TPY-MOL-CoPP (using the spectra at 0.14 V_{RHE} as a reference) under CO_2 atmosphere ($CO_2/NaHCO_3$, 0.1M, pH = 6.8) showed the appearance of a positive peak at 1438 cm^{-1} and a negative peak at 1380 cm^{-1} (Figure 7c), which are assigned to loss of pyridine due to the formation of pyridinium. Such an assignment is confirmed by the very similar DRIFTS spectrum of protonating TPY-MOL-CoPP with HCl (Figure 4b). This pyH^+ feature was not observed for either TPY-MOL-CoPP under N_2 atmosphere (Figure S14) or BTB-MOL-CoPP under CO_2 atmosphere (Figure S15). The positive peaks near 2342 cm^{-1}, and 1597 cm^{-1} were assigned to the consumption of CO_2 and HCO_3^- in the reaction. Only weak IR signals at 1653 cm^{-1} due to the formation of $[\text{CoPP}]^-$ or $[\text{HCoPP}]^0$ were observed in those control experiments (Figures S14-16, Table S6). TPY-MOL without CoPP did not give any differential DRIFTS signal in the potential scan. Based on these results, we propose the formation of $[\text{pyH}^+\text{-}^-\text{O}_2\text{C-CoPP}]^0$ as a key intermediate for TPY-promoted CO_2 activation and reduction.

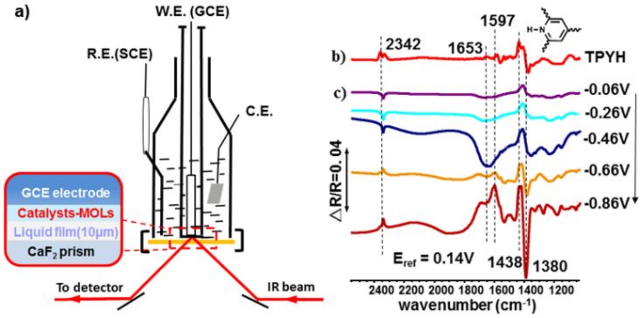

Figure. 7 (a) Schematic of the thin-layer IR cell for the *in-situ* DRIFTS study. (b) IR spectra of TPY-MOL (in H_2O, black line) and TPYH^+-MOL (pH = 4.0 with $HClO_4$, red line). (c) DRIFTS of TPY-MOL-CoPP under the potential scan from -0.06 V_{RHE} to -0.86V_{RHE} in CO_2-saturated aqueous solution of 0.1M $NaHCO_3$. The reference spectrum was taken at 0.14 V_{RHE}.

The signal due to the pyridinium began to show up at the scanning potential around -0.26 V, which coincides with the potential for the reduction of $[\text{CoPP}]^0$ to $[\text{CoPP}]^-$. This is consistent with the formation of the $[\text{pyH}^+\text{-}^-\text{O}_2\text{C-CoPP}]^0$ from the $[\text{CoPP}]^-$, the CO_2, and the pre-assembled pyridine moiety. The DRIFTS signal continues to become more and more prominent upon scanning to more negative potentials. This may indicate the formation of the reduced $[\text{pyH}^+\text{-}^-\text{O}_2\text{C-CoPP}]^-$ species with a DRIFTS signal at similar positions but possibly different intensities as compared with that of $[\text{pyH}^+\text{-}^-\text{O}_2\text{C-CoPP}]^0$(Table S7).

Theoretical Studies and the Catalytic Cycle

We performed theoretical calculations using density functional theory (DFT) in order to reveal key steps for the catalytic cycle (Figures S17-19, Table S9). The pathways for Co-porphyrin catalyzed CO_2RR were established by the works of Koper, Nielsen, and Leung.[36-38] $[\text{CoPP}]^0$ is first reduced to $[\text{CoPP}]^-$ [39] (V_{RHE} = -0.4V by DFT [Figure S20, Table S8 & S9] and -0.28V from experiment [Figure S12]) and then protonated to $[\text{H-CoPP}]^0$ or forming adduct with CO_2 to yield $[\text{HO}_2\text{C-CoPP}]^0$. A further one electron reduction of $[\text{H-CoPP}]^0$ to $[\text{H-CoPP}]^-$ followed by protonation generates H_2 for HER (V_{RHE} = +0.4V by DFT, Figures S20 & S21), while a one electron reduction of $[\text{HO}_2\text{C-CoPP}]^0$ (V_{RHE} = 0.4V by DFT) followed by cleavage of a C-O bond leads to the formation of CO for CO_2RR (Figure 8a, Figure S22).[40]

In this catalytic cycle, the protonation of adsorbed CO_2 has a significant barrier, as indicated by the calculated pKa of 4.2 for $[\text{HO}_2\text{C-CoPP}]^0$, which is disfavored at neutral pH. As a result, the HER path can compete with the CO_2RR for the BTB-MOL-CoPP catalyst, because of the more favorable formation of the $[\text{HCoPP}]^0$ intermediate. A proton-coupled electron transfer pathway at higher overpotential is favored to produce $[\text{HO}_2\text{C-CoPP}]^-$ (Figure 8a). In contrast, the pyridine moiety adjacent to the CoPP center in TPY-MOL-CoPP stabilizes the protonated species $[\text{pyH-O}_2\text{C-CoPP}]^0$. Further injection of the second electron followed by C-O cleavage leads to the CO generation. The proton-coupled electron transfer is still possible to form $[\text{pyH-O}_2\text{C-CoPP}]^-$, but the stepwise protonation / electron transfer path should be competitive for the TPY-MOL-CoPP catalyst.

The pre-assembled cooperative site is critical for the pyridine in stabilizing the $[\text{pyH-O}_2\text{C-CoPP}]^{0/-}$ intermediate. Free pyridine in solution does not promote the formation of such an adduct because of entropy loss of the free pyridine in the process as indicated by DFT calculation (Figure S23). In contrast, the restricted movement of the pre-assembled pyridine decreases the entropy loss to act as a better base, a ubiquitous feature in enzymatic catalysis. Consistent with this conjecture, the addition of 2,6-lutidine, a strong but noncoordinating base, to the solution did not promote the CO_2RR selectivity of the BTB-MOL-CoPP catalyst (Figure 4a). A complete suppression of the translational and rotational entropy of the pyridine moiety leads to a calculated pKa of 16.6 that favors the protonated form at neutral pH, while the free pyridine gives a pKa of 4.2. In our assembly, the CoPP moiety has some flexibility to accommodate the CO_2 substrate, so that the entropy term is not completely suppressed. As a result, we only remove half of the translational entropy of the pyridine to estimate the pKa value (8.5) of the $[\text{pyH-O}_2\text{C-CoPP}]^{0/-}$ intermediate. We also note the possibility of the reduction of protonated terpyridine during the catalytic cycle, which may further facilitate the second electron injection.

We estimated the rate of the second electron transfer following Marcus theory. The electron transfer barrier is assessed by calculating the energies of the reduced or oxidized species at the optimized geometries before and after electron transfer (four energies in total). Crosslinking the four points gives an estimation of the cross point in Marcus theory to obtain the energy barrier (Figure S24). We found that the barrier of the electron transfer is low (approaching 0.01 eV for $[\text{HO}_2\text{C-CoPP}]^{0/-}$ and 0.1 eV for $[\text{pyH-O}_2\text{C-CoPP}]^{0/-}$), suggesting fast electron transfers.

As a result, the cleavage of the C-O bond must be the rate-determining step (RDS). Consistent with this, we observed a large H/D kinetic isotope effect (KIE) for j_{CO} in CO_2RR experiments using $NaDCO_3/CO_2/D_2O$ *vs.* $NaHCO_3/CO_2/H_2O$ solutions. The large $j_{CO\text{-}H}$ / $j_{CO\text{-}D}$ values of 20 for TPY-MOL-CoPP and 14.4 for BTB-MOL-CoPP suggest the potential involvement of H-tunneling in the RDS. We calculated the energy barriers of the C-O breaking steps for the TPY-MOL-CoPP and the BTB-MOL-CoPP. The transition state was found by optimizing the structure with progressively elongated C-O bond length till bond cleavage (Figures S25-28). As our experimental kinetic measurements indicate an additional HCO_3^--assisted pathway, we also calculated the energy barrier with a concerted proton transfer from a HCO_3^- to the hydroxy group in the C-O cleavage. We obtained an activation energy of 1.70 eV for the TPY-MOL-CoPP in the direct C-O bond cleavage pathway and an activation energy of 1.03 eV in the HCO_3^- assisted pathway (Figure 8b), agreeing with the experimental rate law. The transition state of the direct C-O cleavage has a C-O bond length of 2.8 Å while the transition state of the HCO_3^-

-assisted pathway has a C-O bond length of 2.4 Å. Similarly, the activation energy of the BTB-MOL-CoPP is 1.16 eV for the HCO_3^--assisted pathway and is 1.62 eV for the direct bond cleavage pathway (Figure 8b).

Rate Law Based on the Catalytic Cycle

Based on the catalytic cycle with the C-O bond cleavage as the RDS, we can derive the rate laws. For the reaction catalyzed by TPY-MOL-CoPP, $[pyH\text{-}O_2C\text{-}CoPP]^0$ is in equilibrium with $[H\text{-}CoPP]^0$, $[CoPP]^-$, $[O_2C\text{-}CoPP]^-$, and $[HO_2C\text{-}CoPP]^0$ (can be ignored as $[HO_2C\text{-}CoPP]^0 << [pyH\text{-}O_2C\text{-}CoPP]^0$). As a result,

$$[pyH\text{-}O_2C\text{-}CoPP]^0 = [CO_2] / ([CO_2] + K_1 + K_2/[H^+] + K_3[CO_2]/[H^+]) \times [Co] \quad (8)$$

where the [Co] is the total amount of Co sites and K's are the equilibrium constants. From the theoretical calculation, we can obtain $K_1 = 10^{-2.5}$ M and $K_2 = 10^{-9.5}$ M^2, $K_3 = 10^{-8.5}$

There are two paths for the C-O bond cleavage: the bicarbonate-assisted path and the direct path, which leads to the following rate law:

$$j_{CO}/[Co] = (k_1[HCO_3^-] + k_2) \times [pyH\text{-}O_2C\text{-}CoPP]^0 / [Co] = (k_1[HCO_3^-] + k_2) \times [CO_2] / ([CO_2] + K_1 + K_2/[H^+] + K_3[CO_2]/[H^+]) \quad (9)$$

This rate law matches the one from the experimental data when $K_1 >> K_2/[H^+]$, $K_3[CO_2]/[H^+]$. The calculated equilibrium constants are different as compared to those from experimental fitting, mainly due to the difficulty in accurately estimating the entropy term of the pyridine moiety.

For the BTB-MOL-CoPP catalyst, as the formation of $[HO_2C\text{-}CoPP]^0$ is not favorable and a proton-coupled electron transfer pathway is more likely, we consider the $[O_2C\text{-}CoPP]^-$ concentration in equilibrium with the $[H\text{-}CoPP]^0$, $[CoPP]^-$, and $[HO_2C\text{-}CoPP]^0$.

$$[O_2C\text{-}CoPP]^- = [CO_2] / ([CO_2] + K_1' + K_2'[H^+] + K_3'[CO_2][H^+]) \times [Co] \quad (10)$$

Again considering the two paths for the C-O bond cleavage, we can obtain a rate law that matches the one from the experimental data:

$$j_{CO}/[Co] = (k_1'[HCO_3^-] + k_2') \times [O_2C\text{-}CoPP]^- / [Co] = (k_1'[HCO_3^-] + k_2') \times [CO_2] / ([CO_2] + K_1' + K_2'[H^+] + K_3'[CO_2][H^+]) \quad (11)$$

From the theoretical calculation, we obtain $K_1' = 0.1$ M, $K_2' = 10^6$, and $K_3' = 10^{4.2}$ M^{-1} ($K_1' \sim K_2'[H^+] >> K_3'[CO_2][H^+]$). These slightly deviate from the results from experimental fitting, but the general trend is reasonable.

Figure 8 shows the main path of the CO_2RR process catalyzed by the CoPP (Figure 8a, Figures S29 & S30) together with the energy profile of the key steps (Figure 8b) based on the above analyses. The $1e^-$ reduction of CoPP is followed by CO_2 adsorption and protonation to form $[HO_2C\text{-}CoPP]^0$, in competition with the formation of $[H\text{-}CoPP]^0$ that leads to HER. The pre-assembled pyridine moiety stabilizes the $[pyH\text{-}O_2C\text{-}CoPP]^0$ species to favor the CO_2RR path over the HER one in TPY-MOL-CoPP, as shown by the different energies of **3** and **3'** as compared to that of $[H\text{-}CoPP]^0$ in Figure 8b. The RDS in the CO_2RR is the cleavage of the C-O bond after the second electron injection. A HCO_3^--assisted process decreases the energy barrier in the RDS (**6** *vs.* **7** and **6'** *vs.* **7'** in Figure 8b). The pyridinium moiety also changes the energy of the transition state. The release of CO from $[OC\text{-}CoPP]^0$ regenerates the CoPP for catalytic turnover. The pyridinium moiety thus lowers the energy barrier both for CO_2 adsorption and the C-O bond cleavage to promote CO_2RR.

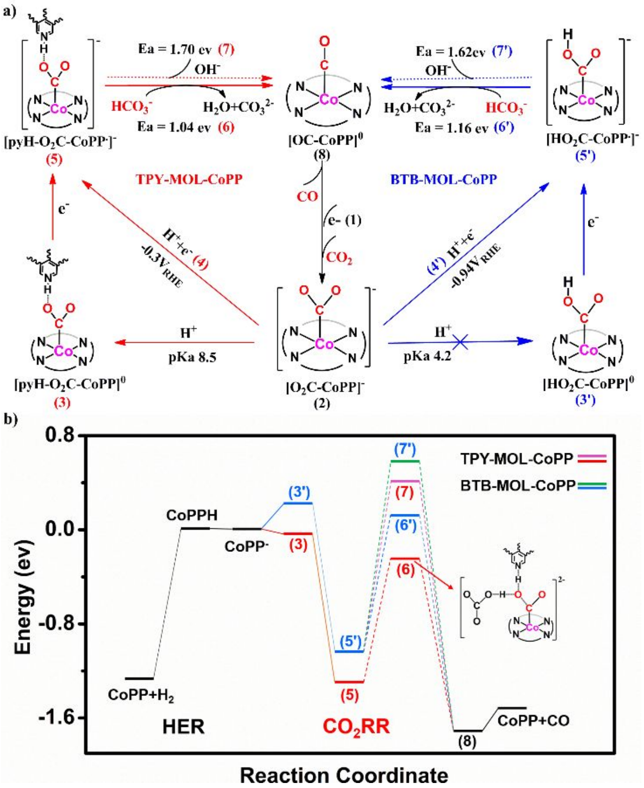

Figure 8. a) Catalytic cycle of CO_2RR by TPY-MOL-CoPP and BTB-MOL-CoPP. The pKa values and redox potentials from DFT calculations are also shown. b) Calculated energy profiles for HER and CO_2RR processes of TPY-MOL-CoPP and BTB-MOL-CoPP.

CONCLUSIONS

In summary, we constructed a catalytic pocket with a CoPP center and a pyridine moiety on a MOL layer for cooperative adsorption and activation of CO_2 for electrochemical CO_2 reduction. The TPY-MOL-CoPP catalyst shows an enhanced CO/H_2 selectivity of 11.8 as compared to a CO/H_2 selectivity of 2.7 for BTB-MOL-CoPP without pyridine. This work highlights unique opportunities in using MOLs as a tunable platform to construct catalytic sites with secondary interactions to enhance product selectivity and to provide mechanistic insights into important electrocatalytic processes.

ASSOCIATED CONTENT

Supporting Information

Experimental details, spectroscopic characterization, DFT calculations and COMSOL simulation. This material is available free of charge via the Internet at http://pubs.acs.org.

AUTHOR INFORMATION

Corresponding Author

* E-mail: wangchengxmu@xmu.edu.cn

Author Contributions

[#] These authors contributed equally.

ACKNOWLEDGMENT

We acknowledge funding support from the National Natural Science Foundation and Ministry of Science and Technology of the P. R. China (NSFC21671162, 2016YFA0200702, NSFC21721001).

REFERENCES

(1) Diercks, C. S.; Liu, Y.; Cordova, K. E.; Yaghi, O. M. The role of reticular chemistry in the design of CO2 reduction catalysts. *Nat. Mater.* **2018**, *17*, 301.

(2) Hu, X. M.; Ronne, M. H.; Pedersen, S. U.; Skrydstrup, T.; Daasbjerg, K. Enhanced Catalytic Activity of Cobalt Porphyrin in CO2 Electroreduction upon Immobilization on Carbon Materials. *Angew. Chem., Int. Ed.* **2017**, *56*, 6468.

(3) Nam, D. H.; Bushuyev, O. S.; Li, J.; De Luna, P.; Seifitokaldani, A.; Dinh, C. T.; Garcia de Arquer, F. P.; Wang, Y.; Liang, Z.; Proppe, A. H.; Tan, C. S.; Todorovic, P.; Shekhah, O.; Gabardo, C. M.; Jo, J. W.; Choi, J.; Choi, M. J.; Baek, S. W.; Kim, J.; Sinton, D.; Kelley, S. O.; Eddaoudi, M.; Sargent, E. H. Metal-Organic Frameworks Mediate Cu Coordination for Selective CO2 Electroreduction. *J. Am. Chem. Soc.* **2018**, *140*, 11378.

(4) Elgrishi, N.; Chambers, M. B.; Wang, X.; Fontecave, M. Molecular polypyridine-based metal complexes as catalysts for the reduction of CO2. *Chem. Soc. Rev.* **2017**, *46*, 761.

(5) Kang, P.; Cheng, C.; Chen, Z.; Schauer, C. K.; Meyer, T. J.; Brookhart, M. Selective electrocatalytic reduction of CO2 to formate by water-stable iridium dihydride pincer complexes. *J. Am. Chem. Soc.* **2012**, *134*, 5500.

(6) Hod, I.; Sampson, M. D.; Deria, P.; Kubiak, C. P.; Farha, O. K.; Hupp, J. T. Fe-Porphyrin-Based Metal–Organic Framework Films as High-Surface Concentration, Heterogeneous Catalysts for Electrochemical Reduction of CO2. *ACS Catal.* **2015**, *5*, 6302.

(7) Takeda, H.; Cometto, C.; Ishitani, O.; Robert, M. Electrons, Photons, Protons and Earth-Abundant Metal Complexes for Molecular Catalysis of CO2 Reduction. *ACS Catal.* **2016**, *7*, 70.

(8) Mariano, R. G.; McKelvey, K.; White, H. S.; Kanan, M. W. Selective increase in CO2 electroreduction activity at grain-boundary surface terminations. *Science (Washington, DC, U. S.)* **2017**, *358*, 1187.

(9) Albo, J.; Beobide, G.; Castaño, P.; Irabien, A. Methanol electrosynthesis from CO 2 at Cu 2 O/ZnO prompted by pyridine-based aqueous solutions. *Journal of CO2 Utilization* **2017**, *18*, 164.

(10) Barton Cole, E.; Lakkaraju, P. S.; Rampulla, D. M.; Morris, A. J.; Abelev, E.; Bocarsly, A. B. Using a One-Electron Shuttle for the Multielectron Reduction of CO2 to Methanol: Kinetic, Mechanistic, and Structural Insights. *J. Am. Chem. Soc.* **2010**, *132*, 11539.

(11) Barton, E. E.; Rampulla, D. M.; Bocarsly, A. B. Selective solar-driven reduction of CO2 to methanol using a catalyzed p-GaP based photoelectrochemical cell. *J. Am. Chem. Soc.* **2008**, *130*, 6342.

(12) Bocarsly, A. B.; Gibson, Q. D.; Morris, A. J.; L'Esperance, R. P.; Detweiler, Z. M.; Lakkaraju, P. S.; Zeitler, E. L.; Shaw, T. W. Comparative Study of Imidazole and Pyridine Catalyzed Reduction of Carbon Dioxide at Illuminated Iron Pyrite Electrodes. *ACS Catal.* **2012**, *2*, 1684.

(13) Fang, Y.; Flake, J. C. Electrochemical Reduction of CO2 at Functionalized Au Electrodes. *J. Am. Chem. Soc.* **2017**, *139*, 3399.

(14) Sharma, P. P.; Wu, J.; Yadav, R. M.; Liu, M.; Wright, C. J.; Tiwary, C. S.; Yakobson, B. I.; Lou, J.; Ajayan, P. M.; Zhou, X. D. Nitrogen-Doped Carbon Nanotube Arrays for High-Efficiency Electrochemical Reduction of CO2: On the Understanding of Defects, Defect Density, and Selectivity. *Angew. Chem., Int. Ed.* **2015**, *54*, 13701.

(15) Pan, Y.; Lin, R.; Chen, Y.; Liu, S.; Zhu, W.; Cao, X.; Chen, W.; Wu, K.; Cheong, W. C.; Wang, Y.; Zheng, L.; Luo, J.; Lin, Y.; Liu, Y.; Liu, C.; Li, J.; Lu, Q.; Chen, X.; Wang, D.; Peng, Q.; Chen, C.; Li, Y. Design of Single-Atom Co-N5 Catalytic Site: A Robust Electrocatalyst for CO2 Reduction with Nearly 100% CO Selectivity and Remarkable Stability. *J. Am. Chem. Soc.* **2018**, *140*, 4218.

(16) Dridi, H.; Comminges, C.; Morais, C.; Meledje, J. C.; Kokoh, K. B.; Costentin, C.; Saveant, J. M. Catalysis and Inhibition in the Electrochemical Reduction of CO2 on Platinum in the Presence of Protonated Pyridine. New Insights into Mechanisms and Products. *J. Am. Chem. Soc.* **2017**, *139*, 13922.

(17) Lim, C. H.; Holder, A. M.; Hynes, J. T.; Musgrave, C. B. Reduction of CO2 to methanol catalyzed by a biomimetic organo-hydride produced from pyridine. *J. Am. Chem. Soc.* **2014**, *136*, 16081.

(18) Senftle, T. P.; Lessio, M.; Carter, E. A. The Role of Surface-Bound Dihydropyridine Analogues in Pyridine-Catalyzed CO2 Reduction over Semiconductor Photoelectrodes. *ACS. Cent. Sci.* **2017**, *3*, 968.

(19) Yan, Y.; Zeitler, E. L.; Gu, J.; Hu, Y.; Bocarsly, A. B. Electrochemistry of aqueous pyridinium: exploration of a key aspect of electrocatalytic reduction of CO2 to methanol. *J. Am. Chem. Soc.* **2013**, *135*, 14020.

(20) Keith, J. A.; Carter, E. A. Theoretical Insights into Electrochemical CO2 Reduction Mechanisms Catalyzed by Surface-Bound Nitrogen Heterocycles. *The Journal of Physical Chemistry Letters* **2013**, *4*, 4058.

(21) Campbell, M. G.; Liu, S. F.; Swager, T. M.; Dinca, M. Chemiresistive Sensor Arrays from Conductive 2D Metal-Organic Frameworks. *J. Am. Chem. Soc.* **2015**, *137*, 13780.

(22) Zhao, M.; Lu, Q.; Ma, Q.; Zhang, H. Two-Dimensional Metal-Organic Framework Nanosheets. *Small Methods* **2017**, *1*, 1600030.

(23) Cao, L.; Lin, Z.; Peng, F.; Wang, W.; Huang, R.; Wang, C.; Yan, J.; Liang, J.; Zhang, Z.; Zhang, T.; Long, L.; Sun, J.; Lin, W. Self-Supporting Metal-Organic Layers as Single-Site Solid Catalysts. *Angew. Chem., Int. Ed.* **2016**, *55*, 4962.

(24) Wang, T.; Zeng, Z.; Cao, L.; Li, Z.; Hu, X.; An, B.; Wang, C.; Lin, W. A Dynamically Stabilized Single-Nickel Electrocatalyst for Selective Reduction of Oxygen to Hydrogen Peroxide. *Chem. - Eur. J.* **2018**, *24*, 17011.

(25) Zhao, S.; Wang, Y.; Dong, J.; He, C.-T.; Yin, H.; An, P.; Zhao, K.; Zhang, X.; Gao, C.; Zhang, L.; Lv, J.; Wang, J.; Zhang, J.; Khattak, A. M.; Ali Khan, N.; Wei, Z.; Zhang, J.; Liu, S.; Zhao, H.; Tang, Z. Ultrathin metal-organic framework nanosheets for electrocatalytic oxygen evolution. *Nat. Energy* **2016**, *1*, 16184.

(26) Shi, W.; Cao, L.; Zhang, H.; Zhou, X.; An, B.; Lin, Z.; Dai, R.; Li, J.; Wang, C.; Lin, W. Surface Modification of Two-Dimensional Metal-Organic Layers Creates Biomimetic Catalytic Microenvironments for Selective Oxidation. *Angew. Chem., Int. Ed.* **2017**, *56*, 9704.

(27) Monti, D.; Ottolina, G.; Carrea, G.; Riva, S. Redox reactions catalyzed by isolated enzymes. *Chem. Rev.* **2011**, *111*, 4111.

(28) Wang, Z. J.; Clary, K. N.; Bergman, R. G.; Raymond, K. N.; Toste, F. D. A supramolecular approach to combining enzymatic and transition metal catalysis. *Nat. Chem.* **2013**, *5*, 100.

(29) Lin, S.; Nichols, E. M.; Diercks, C. S.; Zhang, Y.-B.; Kornienko, N.; Zhao, Y.; Paris, A. R.; Kim, D.; Yang, P.; Yaghi, O. M.; Chang, C. J. Covalent organic frameworks comprising cobalt porphyrins for catalytic CO2 reduction in water. *Science* **2015**, *349*, 1208.

(30) Diercks, C. S.; Lin, S.; Kornienko, N.; Kapustin, E. A.; Nichols, E. M.; Zhu, C.; Zhao, Y.; Chang, C. J.; Yaghi, O. M. Reticular Electronic Tuning of Porphyrin Active Sites in Covalent Organic Frameworks for Electrocatalytic Carbon Dioxide Reduction. *J. Am. Chem. Soc.* **2018**, *140*, 1116.

(31) Kornienko, N.; Zhao, Y.; Kley, C. S.; Zhu, C.; Kim, D.; Lin, S.; Chang, C. J.; Yaghi, O. M.; Yang, P. Metal-organic frameworks for electrocatalytic reduction of carbon dioxide. *J. Am. Chem. Soc.* **2015**, *137*, 14129.

(32) Singh, M. R.; Kwon, Y.; Lum, Y.; Ager, J. W., 3rd; Bell, A. T. Hydrolysis of Electrolyte Cations Enhances the Electrochemical Reduction of CO2 over Ag and Cu. *J. Am. Chem. Soc.* **2016**, *138*, 13006.

(33) Dunwell, M.; Yang, X.; Setzler, B. P.; Anibal, J.; Yan, Y.; Xu, B. Examination of Near-Electrode Concentration Gradients and Kinetic Impacts on the Electrochemical Reduction of CO2 using Surface-Enhanced Infrared Spectroscopy. *ACS Catal.* **2018**, *8*, 3999.

(34) Tobias, C. W.; Eisenberg, M.; Wilke, C. R. Diffusion and convection in electrolysis-a theoretical review. *J. Electrochem. Soc.* **1952**, *99*, 359C.

(35) Singh, M. R.; Clark, E. L.; Bell, A. T. Effects of electrolyte, catalyst, and membrane composition and operating conditions on the performance of solar-driven electrochemical reduction of carbon dioxide. *Physical Chemistry Chemical Physics* **2015**, *17*, 18924.

(36) Gottle, A. J.; Koper, M. T. M. Determinant Role of Electrogenerated Reactive Nucleophilic Species on Selectivity during

Reduction of CO2 Catalyzed by Metalloporphyrins. *J. Am. Chem. Soc.* **2018**, *140*, 4826.

(37) Gottle, A. J.; Koper, M. T. M. Proton-coupled electron transfer in the electrocatalysis of CO2 reduction: prediction of sequential vs. concerted pathways using DFT. *Chem. Sci.* **2017**, *8*, 458.

(38) Leung, K.; Nielsen, I. M. B.; Sai, N.; Medforth, C.; Shelnutt, J. A. Cobalt-porphyrin catalyzed electrochemical reduction of carbon dioxide in water. 2. Mechanism from first principles. *J. Phys. Chem. A.* **2010**, *114*, 10174.

(39) de Groot, M. T.; Koper, M. T. Redox transitions of chromium, manganese, iron, cobalt and nickel protoporphyrins in aqueous solution. *PCCP* **2008**, *10*, 1023.

(40) Shen, J.; Kortlever, R.; Kas, R.; Birdja, Y. Y.; Diaz-Morales, O.; Kwon, Y.; Ledezma-Yanez, I.; Schouten, K. J.; Mul, G.; Koper, M. T. Electrocatalytic reduction of carbon dioxide to carbon monoxide and methane at an immobilized cobalt protoporphyrin. *Nat. Commun.* **2015**, *6*, 8177.